ADVANCED FUNCTIONAL MATERIALS
www.afm-journal.de

Materials Views
www.MaterialsViews.com

FULL PAPER

Bioinspired Scaffolds with Varying Pore Architectures and Mechanical Properties

Michael M. Porter, Russ Imperio, Matthew Wen, Marc A. Meyers, and Joanna McKittrick*

Scaffolds with potential biological applications having a variety of microstructural and mechanical properties can be fabricated by freezing colloidal solutions into porous solids. In this work, the structural and mechanical properties of TiO_2 freeze cast with different soluble additives, including polyethylene glycol, NaOH or HCl, and isopropanol alcohol, are characterized to determine the effects of slurry viscosity, pH, and alcohol concentration on the freezing process. TiO_2 powders mixed with water and these different additives are directionally frozen in a mold, then sublimated and sintered to create the porous scaffolds. The different scaffolds are characterized to compare the compressive strength, modulus, porosity, and pore morphology. For all scaffolds, the overall porosity remains constant (80–85%). By changing the concentration of each additive, the lamellar thickness, pore area, and aspect ratio vary significantly, showing inverse relationships to both the compressive strength and modulus. The strength is predicted from the pore aspect ratio of the scaffolds when subjected to compressive loading with the primary failure mode identified as Euler buckling. TiO_2 scaffolds freeze cast with different soluble additives are suitable for biomedical applications, such as bone replacements, requiring high porosity and specific pore morphologies.

1. Introduction

Attempts to replicate the microstructures of biological materials, such as bone and nacre, have long been the focus of intense study due to their robust mechanical properties and moderate density, despite being comprised of relatively weak constituents.[1] This combination of properties is advantageous for the aerospace, automotive, and, especially, biomedical industries, with the possibility of fabricating synthetic bone replacements.[1–4] The microstructure of bone is highly anisotropic and requires specific levels of open porosity for the presence of living tissues, cells, and fluids.[5] An ideal bone replacement should have an open porosity and mechanical properties similar to those of natural bone.[6] However, a common challenge in manufacturing porous structures is maintaining desired levels of compressive strength and stiffness while generating specific levels of open porosity with optimal pore morphologies.

Freeze casting is a fabrication method that allows for fine microstructural control during the synthesis of porous ceramic scaffolds or hybrid composites (upon infiltration of a second phase) with physical and mechanical properties similar to natural bone.[2–4] It involves directionally freezing a liquid slurry comprised of a solvent, ceramic powder, dispersant and binder (the latter two are for even particle distribution and green body integrity, respectively).[4] After freezing, the solvent crystals are sublimated by freeze drying, resulting in lamellar pore channels that are direct replicas of the frozen solvent. Afterwards, the ceramic scaffold is sintered to partially densify and strengthen the porous construct.

Numerous studies have been conducted using different ceramic powders and liquid solvents with observed changes in the microstructure and compressive behavior of various ceramic scaffolds fabricated by freeze casting.[4,7,8] The overall porosity of a scaffold is directly dependent on the amount of solid loading in the slurry, while the pore size and morphology can be controlled by changing the processing conditions.[9] Microstructural properties, such as the composition and thickness of lamellar columns, amount of bridging between the columns, surface roughness and pore geometry are some of the most important mechanisms that affect the mechanical performance.[3,9] Several works have analyzed these structural parameters, which may be induced by the addition of soluble additives, such as polyethylene glycol (PEG),[10] polyvinyl alcohol (PVA),[11] sucrose, ethanol, sodium chloride,[12] glycerol, dioxane,[13] and zirconium acetate.[14] Many soluble additives generate significant changes in the pore size and morphology, as they have an observed effect on the solidification temperature, freezing-front velocity, and crystal formation in the liquid slurry.[10–14] For example, different chemical additives were found by Munch et al.[12] to alter the solidification temperature of the slurry. Regardless of the obvious architectural differences, the spacing of the pores was directly related to the freezing-front velocity,

M. M. Porter, Prof. M. A. Meyers, Prof. J. McKittrick,
Materials Science and Engineering Program
University of California
San Diego, 9500 Gilman Drive, La Jolla, CA, 92093, USA
E-mail: m1porter@ucsd.edu
R. Imperio, M. Wen, Prof. M. A. Meyers,
Prof. J. McKittrick
Department of Mechanical and Aerospace Engineering
University of California
San Diego, 9500 Gilman Drive, La Jolla, CA, 92093, USA
Prof. M. A. Meyers
Department of NanoEngineering
University of California
San Diego, 9500 Gilman Drive, La Jolla, CA, 92093, USA

DOI: 10.1002/adfm.201302958

independent of the additives used.[12] Similarly, Deville et al.[14] showed that the evolution of pores is dependent on the growth velocity and driving force of crystal formation, through the use of various ice-structuring compounds. The pore structures in these works were shown to be cellular, lamellar, columnar, faceted, dendritic, hopper, or polyhedral in nature.[12–14]

Rheological properties of freeze cast slurries have also been shown to influence the pore morphology of the resulting scaffolds without changing their overall porosity. Parameters such as the viscosity and pH influence the dispersion homogeneity and stability of ceramic particles in aqueous solutions.[15–17] During the freezing process particles are either rejected or entrapped by the approaching freezing front—a function of the thermodynamic free energy of the system and constitutional supercooling, as described by Wegst et al.[18] and Deville et al.[19] Therefore, to avoid significant particle agglomeration and/or segregation during the freezing process, it is important to determine the optimal viscosity and pH of the slurry for a desired pore morphology.[16] Different types and concentrations of dispersants have been added to significantly lower the slurry viscosity for better defined pore structures.[15–17] Likewise, the pH can be adjusted so that the electric potential of the colloidal solution is stable.[16,17] Along with other processing parameters, including the freezing rate and sintering conditions, these liquid properties are easily controlled and have a profound effect on the final pore architecture and resulting mechanical performance.[15,20,21] Finely-tailored pore architectures can be designed for specific applications, for example osteogenesis or bone ingrowth, by utilizing a variety of liquid additives.

Here we demonstrate the effect of slurry viscosity, pH, and alcohol concentration on the structural and mechanical properties associated with porous TiO_2 scaffolds, which are promising and relatively untested ceramic constructs produced by freeze casting. To the best of our knowledge, Ren et al.[22–24] and Porter et al.[25] provide the only other reports on freeze cast TiO_2 to date. Although it has been shown that TiO_2 is a suitable material for freeze casting porous anisotropic scaffolds,[25] the structural and mechanical properties of TiO_2 freeze cast with various liquid additives has not yet been reported. Altering the viscosity, pH and alcohol concentration may allow for the modification of the porous microstructures to meet the criteria of various applications, specifically by altering the pore size and shape without changing the overall porosity. This is the first empirical analysis on the effect different rheological properties in the liquid slurry (i.e., viscosity, pH, alcohol concentration) have on the microstructure and mechanical properties of freeze cast TiO_2. Unlike other works that investigate the slurry viscosity by altering the concentration of dispersants,[15–17] we use equal concentrations of a soluble polymer (PEG) with varying molecular weights or varying concentrations of a liquid additive (isopropanol alcohol (IPA)) to change the liquid properties of the ceramic slurries. Quantitative measurements of the porosity, pore morphology, lamellar architecture, and compressive mechanical properties of the freeze cast scaffolds are systematically compared for each of the conditions investigated. A simplified analysis of Euler buckling is used to describe the principal failure mechanisms of these scaffolds when subjected to compressive loading.

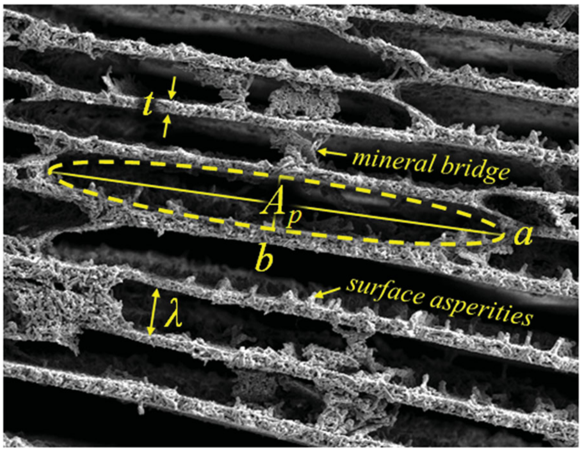

Figure 1. Representative image of a freeze cast TiO_2 scaffold illustrating the different microstructural features and measurements: mineral bridges connecting adjacent lamellar walls; surface asperities creating a characteristic wall roughness; fitted ellipse (dashed line): pore area (A_p), major axis (a), and minor axis (b); interlamellar spacing ($\lambda = b$), and lamellar thickness (t).

2. Results and Discussion

2.1. Scaffold Characterization

Several TiO_2 scaffolds with equal porosity (≈80–85%) were fabricated by directionally freezing three sets of colloidal solutions with different rheological properties by changing the following parameters: 1) viscosity, controlled by adding 1 wt% of PEG with varying molecular weights (0–20 000); 2) pH change, controlled by adding small amounts of HCl or NaOH to respectively decrease or increase the slurry pH (2–12); 3) alcohol concentration, controlled by adding varying concentrations of IPA (0–30 vol%).

After freezing, the samples were lyophilized, then sintered at 1000 °C. X-ray diffraction (XRD) confirmed that the crystal structures of all the TiO_2 scaffolds transformed from anatase before sintering to rutile after sintering.

Figure 1 shows a representative scanning electron microscopy (SEM) image of the different structural features and measurements investigated, where the ice growth direction is out of the page. To compare the different scaffolds, **Tables 1–3** contain the slurry properties, pore morphologies, and compressive mechanical properties for each of the three experimental sets. The overall porosity (ϕ) of the scaffolds were measured by mass (m) and volume (V) with respect to that of fully dense TiO_2 ($\rho_{TiO2} = 4.26$ g cm^{-3}), as shown:

$$\rho_{rel} = \frac{\rho}{\rho_{TiO_2}} = \frac{m/V}{\rho_{TiO_2}} \tag{1}$$

$$\phi = (1 - \rho_{rel}) \times 100\% \tag{2}$$

where ρ_{rel} is the relative density and $\rho = m/V$ is the measured sample density. The pore area (A_p) was calculated from the elliptic major (a) and minor (b) axes according to Figure 1 (refer to Experimental Section for more detail):

$$A_p = \frac{\pi}{4} ab \tag{3}$$

The pore aspect ratio (χ_p) is a measure of the pore morphology and was calculated from the elliptic major (a) and minor (b) axes as follows:

$$\chi_p = \frac{a}{b} \tag{4}$$

Although the overall porosity of the different scaffolds remained nearly constant (≈80–85%), the pore size and shape changed dramatically, with pore areas ranging from ≈200 μm^2 to ≈5000 μm^2 and aspect ratios ranging from ≈2 to ≈10. Accordingly, the lamellar wall thickness (t) and length (major axis, a) varied from ≈2 μm to ≈20 μm and ≈20 μm to ≈250 μm, respectively. The interlamellar spacing (λ) of the scaffold walls, which is equivalent to the minor axis ($\lambda = b$) noted above, varied from ≈10 μm to ≈20 μm. This parameter was determined by Deville et al.[26] to be inversely proportional to the freezing front velocity (v), following the power law:

$$\lambda \propto \frac{1}{v^n} \tag{5}$$

Table 1. Slurry properties (viscosity, pH), pore morphology (porosity, pore area, major and minor axes, aspect ratio, lamellar thickness), and compressive mechanical properties (strength, modulus) of TiO_2 scaffolds freeze cast with 1 wt% polyethylene glycol (PEG) of varying molecular weights (MW).

PEG (MW)	0	2000	10 000	20 000
Viscosity, μ [mPa s]	1.44 ± 0.02	1.50 ± 0.03	1.63 ± 0.02	1.75 ± 0.02
pH	≈ 7	≈ 7	≈ 7	≈ 7
Overall porosity, ϕ [%]	82.1 ± 0.9	82.8 ± 0.3	83.2 ± 0.1	83.7 ± 0.4
Pore area, A_p [μm^2]	465 ± 234	302 ± 54	234 ± 36	531 ± 82
Pore major axis, a [μm]	37 ± 32	30 ± 15	29 ± 14	49 ± 28
Pore minor axis, b [μm]	16 ± 9	13 ± 5	10 ± 3	14 ± 4
Pore aspect ratio, χ_p	2.36	2.33	2.74	3.52
Lamellar thickness, t [μm]	3.69 ± 1.85	4.06 ± 2.86	2.54 ± 1.27	2.87 ± 1.67
Strength, σ [MPa]	4.4 ± 0.3	6.1 ± 0.4	6.7 ± 0.2	3.0 ± 0.4
Modulus, E [MPa]	309 ± 125	616 ± 194	662 ± 162	327 ± 123

All data shown as average ± standard deviation.

Table 2. Slurry properties (viscosity, pH), pore morphology (porosity, pore area, major and minor axes, aspect ratio, lamellar thickness), and compressive mechanical properties (strength, modulus) of TiO_2 scaffolds freeze cast with varying pH by adding various concentrations of HCl or NaOH to increase or decrease the pH of the slurry, respectively.

HCl or NaOH [m]	0.036 (HCl)	0.024 (HCl)	0.012 (HCl)	0.002 (NaOH)	0.004 (NaOH)	0.006 (NaOH)
Viscosity, μ [mPa s]	1.59 ± 0.04	1.66 ± 0.02	1.60 ± 0.03	1.61 ± 0.03	1.59 ± 0.02	1.62 ± 0.04
pH	≈ 2	≈ 4	≈ 6	≈ 8	≈ 10	≈ 12
Overall porosity, ϕ [%]	85.5 ± 0.6	83.7 ± 1.2	84.5 ± 0.2	84.0 ± 0.4	84.8 ± 0.3	85.7 ± 0.1
Pore area, A_p [μm^2]	3332 ± 492	1673 ± 561	544 ± 145	186 ± 47	351 ± 111	929 ± 126
Pore major axis, a [μm]	154 ± 92	97 ± 90	57 ± 38	23 ± 13	36 ± 27	64 ± 33
Pore minor axis, b [μm]	28 ± 7	22 ± 8	12 ± 5	10 ± 5	12 ± 5	18 ± 5
Pore aspect ratio, χ_p	5.59	4.45	4.77	2.15	2.94	3.47
Lamellar thickness, t [μm]	17.73 ± 9.43	12.12 ± 6.66	6.32 ± 3.40	3.13 ± 2.76	3.86 ± 2.25	5.13 ± 2.71
Strength, σ [MPa]	4.8 ± 0.8	6.6 ± 0.5	5.4 ± 0.4	9.5 ± 0.4	7.2 ± 0.6	7.1 ± 0.8
Modulus, E [MPa]	301 ± 54	415 ± 52	442 ± 80	621 ± 229	496 ± 77	582 ± 174

All data shown as average ± standard deviation.

Table 3. Slurry properties (viscosity, pH), pore morphology (porosity, pore area, major and minor axes, aspect ratio, lamellar thickness), and compressive mechanical properties (strength, modulus) of TiO_2 scaffolds freeze cast with varying concentrations of isopropanol alcohol (IPA).

IPA [vol%]	0	1	5	15	30
Viscosity, μ [mPa s]	1.63 ± 0.02	2.18 ± 0.06	2.05 ± 0.05	3.04 ± 0.03	4.67 ± 0.10
pH	≈ 7	≈ 7	≈ 7	≈ 7	≈ 7
Overall porosity, ϕ [%]	83.2 ± 0.1	84.6 ± 0.2	84.8 ± 0.2	83.1 ± 0.3	78.9 ± 1.1
Pore area, A_p [μm^2]	234 ± 36	2330 ± 556	4876 ± 1153	2778 ± 188	612 ± 146
Pore major axis, a [μm]	29 ± 14	158 ± 106	244 ± 197	170 ± 69	72 ± 44
Pore minor axis, b [μm]	10 ± 3	19 ± 7	25 ± 7	21 ± 3	11 ± 4
Pore aspect ratio, χ_p	2.74	8.46	9.61	8.17	6.67
Lamellar thickness, t [μm]	2.54 ± 1.27	6.72 ± 4.04	15.71 ± 12.85	10.39 ± 6.62	4.53 ± 2.62
Strength, σ [MPa]	6.7 ± 0.2	3.3 ± 0.3	0.7 ± 0.1	1.3 ± 0.3	1.0 ± 0.2
Modulus, E [MPa]	662 ± 162	263 ± 55	90 ± 38	176 ± 51	132 ± 38

All data shown as average ± standard deviation.

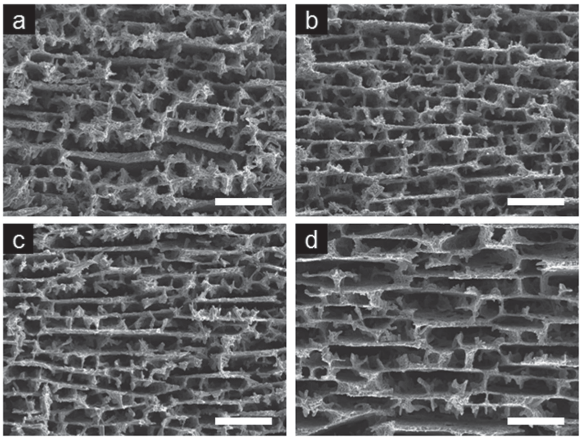

Figure 2. Scanning electron micrographs of TiO_2 scaffolds freeze cast with 1 wt% polyethylene glycol (PEG) of varying molecular weight (MW) and solution viscosity: a) 0 wt% PEG, 1.44 mPa s; b) 2000 MW, 1.50 mPa s; c) 10,000 MW, 1.63 mPa s; d) 20,000 MW, 1.75 mPa s. Scale bars: 50 μm.

where *n* is related to the colloidal particle size and should be equal for all experiments reported here. Therefore, it can be assumed that the small variation in the interlamellar spacing is caused by the different slurry properties, which may affect the freezing front velocity. Regardless, the major structural changes observed in the different scaffolds were the lamellar thickness, pore area, pore aspect ratio, and compressive mechanical properties, which are discussed in more detail below.

2.2. Viscosity

Adding PEG to the freeze cast slurries and increasing its molecular weight increased the viscosity of the slurries without changing the overall porosity of the scaffolds (see Table 1). However, the different molecular weights of PEG added to the slurries resulted in variations in pore area, surface roughness, lamellar bridging, and channel alignment. These structural parameters were observed to have a pronounced effect on the mechanical properties. **Figures 2**,**3** compare, respectively, SEM images and the structural and mechanical properties of the scaffolds fabricated with varying slurry viscosities. During freezing, ice crystal formation generated successive layers of scaffolding along the ice growth direction (out of the page, Figure 2). Secondary dendrites produced irregularities in the scaffolds as the solidification front progressed, resulting in characteristic surface roughness, similar to PEG experiments reported by Pekor et al.[10] Referring to Figure 3a, a slight variation in the pore area (200–600 μm^2) was observed, while the overall porosity (≈85%) of the scaffolds remained constant. The pore channels in the scaffolds made with no PEG are cellular with less homogeneous alignment, higher surface roughness, and dense mineral bridging (see Figure 2a). Conversely, the pore channels in the scaffolds made with the highest molecular weight PEG are more homogeneously aligned with lower surface roughness and less mineral bridging (see Figure 2d).

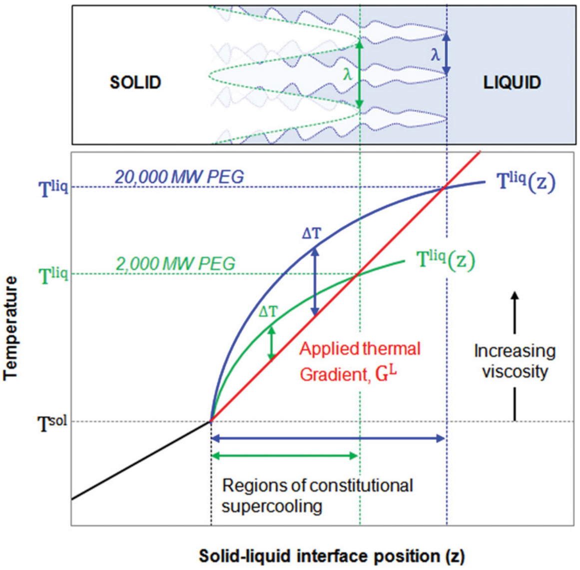

Figure 4. Thermal profiles of water–PEG solutions as a function of the position across the solid–liquid interface. The blue curve represents PEG solutions with a high molecular weight (e.g., 20 000) and higher freezing temperature, resulting in columnar dendritic-like structures. The green curve represents PEG solutions with a low molecular weight (e.g., 2000) and lower freezing temperature, resulting in more cellular-like structures. The diagram above illustrates the transition from cellular (green) to dendritic (blue) crystal structures. The two curves in the diagram illustrate that there is a larger region of constitutional supercooling, $\Delta T \sim \frac{A}{\lambda}$, for water–PEG solutions with higher viscosities, resulting in finer instabilities.

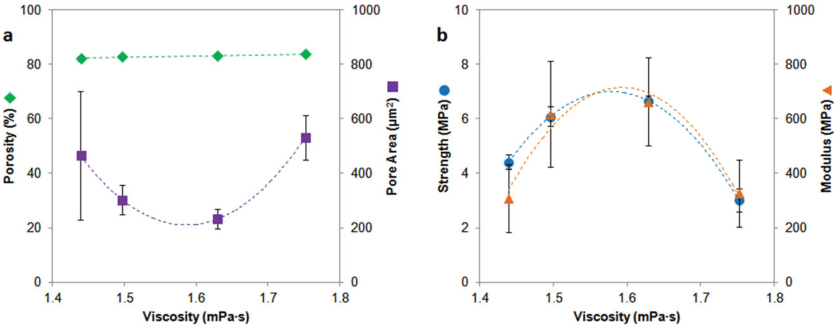

Figure 3. Comparison of a) porosity (green, diamonds), pore area (purple, squares), b) compressive strength (blue, circles), and compressive modulus (orange, triangles) for TiO_2 scaffolds freeze cast with varying viscosity by addition of polyethylene glycol (PEG) with different molecular weights.

Although, the addition of PEG initially lowers the freezing temperature of water–PEG solutions to below 0 °C, increasing the viscosity (with higher molecular weight PEG) increases the freezing temperature of the PEG-modified slurries. **Figure 4** contains a diagram of expected thermal profiles for different water–PEG solutions at the solid–liquid interface (i.e., freezing front). As seen in the diagram, the region of constitutional supercooling is greater for solutions with higher molecular weights, and thereby,

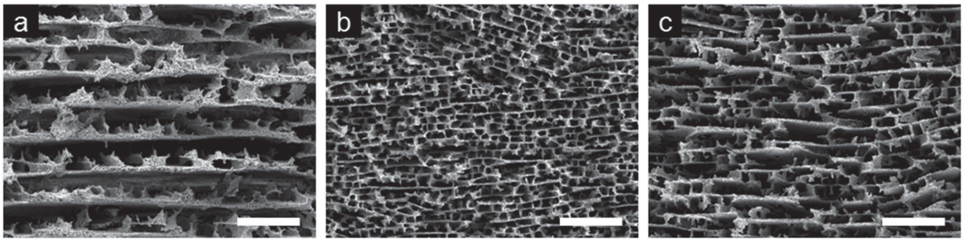

Figure 5. Scanning electron micrographs of TiO_2 scaffolds freeze cast with varying pH: a) pH 2; b) pH 7; c) pH 12. Scale bars: 100 µm.

higher viscosities. This increase in viscosity leads to a larger amount of constitutional supercooling, ΔT:[27]

$$\Delta T \sim \frac{A}{\lambda} \tag{6}$$

where A is a materials constant and λ is the lamellar spacing, which is directly related to the local curvature of instabilities at the solid–liquid interface. Constitutional supercooling occurs when the applied thermal gradient in the liquid (G^L) is less than the equilibrium thermodynamic temperature of the liquid (refer to Figure 4):[28]

$$G^L < \frac{v}{D}\left(T^{\text{liq}} - T^{\text{sol}}\right) \tag{7}$$

where v is the freezing front velocity, D is the mass diffusivity of the liquid, T^{liq} is the equilibrium liquidus temperature, and T^{sol} is the equilibrium solidus temperature. When no supercooling exists in the solution, the solid–liquid interface is considered stable and planar.[28] At low viscosity the amount of supercooling is small, leading to a slow freezing front velocity and the growth of cellular ice crystals.[28] In contrast, a larger region of supercooling at higher viscosity leads to a faster freezing front velocity and the formation of dendritic ice crystals.[28] Therefore, scaffolds made from the slurry with the lowest viscosity (≈1.50 mPa s) contain smaller cellular pore structures (Figure 2b), while those made from the highest viscosity (≈1.75 mPa s) contain larger lamellar pores (Figure 2d). If the viscosity is increased even further (beyond ≈2 mPa s), the dendritic crystals should become finer, resulting in a reduced lamellar spacing. This phenomenon is discussed in more detail in Section 2.4, where the addition of IPA increases the viscosity beyond ≈2 mPa s.

Referring to Figure 3, both the compressive strength and modulus are inversely related to the pore area. An optimal viscosity of ≈1.6 mPa s leads to a minimum pore area and maximum compressive mechanical properties. Beyond this point (≈1.6 mPa s), the pore area increases as the viscosity increases. This is likely due to the tendency of TiO_2 particles interacting with the longer-chain PEG molecules to aggregate as they are rejected by the solidification front. The smaller, more homogeneous pore channels (Figure 2b,c) with low aspect ratios (≈2.5) displayed the highest compressive strength (≈6 MPa) and modulus (≈600 MPa) at a liquid viscosity of ≈1.6 mPa s. This observed structure-property relationship agrees with hypotheses presented by Hunger et al.,[9] suggesting that decreased lamellar spacing and reduced aspect ratio lead to enhanced mechanical performance. For this reason, 1 wt% PEG with a molecular weight of 10 000 (≈1.6 mPa s) was added to all of the slurries of the remaining experiments, detailed in the following sections.

2.3. pH Change

In contrast to changes in viscosity, variations in the pH of the slurries had a more significant effect on the pore area (200–4000 µm^2) of the microstructures, while the overall porosity (≈85%) remained constant (**Table 2**). The slurries with changing pH showed nearly equal viscosities (Table 2). **Figure 5** compares SEM micrographs of the scaffolds made from slurries at pH 2, 7, and 12. **Figure 6** compares the porosity, pore area, and compressive mechanical properties of scaffolds made from slurries at different pH levels. As seen in Figure 5, the channel lengths, widths, and general morphologies vary considerably with changing pH. At low pH (≈2) the lamellar surfaces have a coarse roughness and low density of bridging, due to the increased spacing and thickness of lamellae. This results in a large variation in pore area (refer to error bars, Figure 6a). It appears that a low pH induces more elongated pores, with aspect ratios of ≈5 (see Table 2). As the pH increases from 2 to 7 the pore area reduces significantly from values of 4000 µm^2 at pH 2 (Figure 5a) to 250 µm^2 at pH 7 (Figure 5b). At neutral pH a fine network of pores evolves from tiny homogeneously distributed ice crystals. As the pH increases from 7 to

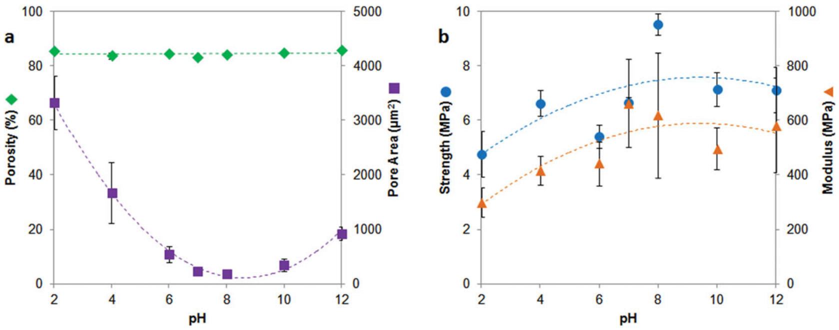

Figure 6. Comparison of a) porosity (green, diamonds), pore area (purple, squares), b) compressive strength (blue, circles), and compressive modulus (orange, triangles) for TiO_2 scaffolds freeze cast with varying pH.

12 there is only a slight increase in the pore area, approaching values of 1000 µm^2 at pH 12 (Figure 5c). A high pH has only moderate effects on lamellar wall spacing, thus allowing some bridging of the walls.

In agreement with Zhang et al.,[16] there was a significant variation in the pore architecture at different pH levels. However, the dispersion of particles in the suspension seemed stable at all pH levels, resulting in well-defined pore structures. The presence hydrogen, hydronium, or hydroxide groups may decrease the solidification temperature in the solvent, thereby slowing the ice crystal growth velocity,[26] similar to the effect of ice-structuring compounds investigated by Deville et al.[14] The resulting effect of a decreased freezing front velocity is the presence of larger, faceted pores in the lamellar microstructure as the region of constitutional supercooling is smaller and water molecules are more slowly incorporated into the ice crystals, causing an increase in their average size and aspect ratio.[14]

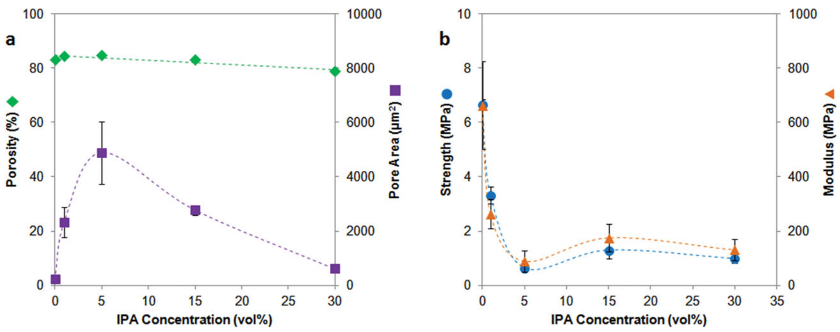

Figure 8. Comparison of a) porosity (green, diamonds), pore area (purple, squares), b) compressive strength (blue, circles), and compressive modulus (orange, triangles) for TiO_2 scaffolds freeze cast with varying isopropanol alcohol (IPA) concentrations.

Similar to the viscosity experiments, the compressive mechanical properties follow a loose inverse relationship with the pore area, with strengths ranging from 4–10 MPa and stiffnesses ranging from 200–800 MPa. The highest strength (≈9 MPa) and stiffness (≈600 MPa) occur in scaffolds with the lowest pore area (≈200 µm^2) and aspect ratio (≈2) at pH ≈ 8.

2.4. Alcohol Concentration

Modification of alcohol (IPA) concentration in the slurries generated scaffolds that are vastly different from those freeze cast with changing viscosity and pH. **Figures 7**,**8** show SEM images and plots, respectively, of the structural and mechanical properties of the scaffolds freeze cast with increasing concentrations of IPA. The addition of IPA to the slurries increased the viscosity significantly; however, the pH remained neutral (≈7) (see Table 3). As seen in Figure 7a, the pore area increases dramatically, then slowly decreases as the alcohol concentration is further increased. In comparison, scaffolds freeze cast with changing viscosity and pH had more boxy, rectangular pores (Figures 2,5), while the addition of alcohol led to more elongated pore channels (Figure 7) with high aspect ratios, up to ≈10 (Table 3). Furthermore, scaffolds freeze cast with IPA showed some extent of finer periodic surface features (see Figure 7). The different pore morphologies coincide with an increase of the maximum pore area and aspect ratio, respectively, to ≈6000 µm^2 and ≈10 for IPA-modified slurries, compared to ≈4000 µm^2 and ≈5.5 for pH-modified slurries, and ≈600 µm^2 and ≈3.5 for viscosity-modified slurries. As the alcohol concentration was increased beyond 5 vol% there is very little change in the porosity, compressive strength and stiffness. However, the dramatic increase in viscosity above ≈2 mPa s (see Table 3) led to finer instabilities in the solid–liquid interface, resulting in smaller pore sizes and reduced lamellar spacing (refer to Figure 4).

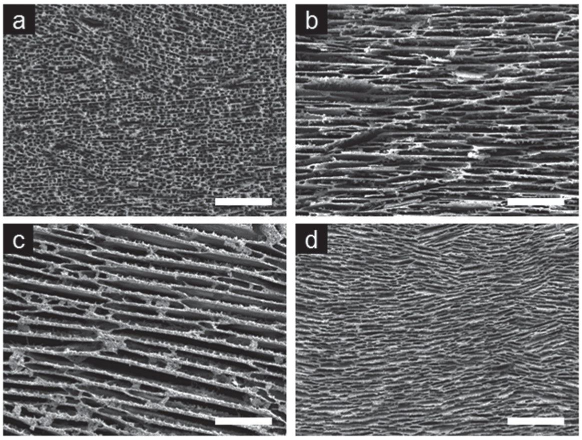

Figure 7. Scanning electron micrographs of TiO_2 scaffolds freeze cast with varying concentrations of isopropanol alcohol (IPA): a) 0 vol%; b) 1 vol%; c) 5 vol%; d) 30 vol%. Scale bars: 200 µm.

The maximum pore area observed at 5 vol% IPA is likely due to an interaction between IPA and water that favors crystallization, producing large elongated pore channels (Figure 7c). Similar to observations made by Munch et al.[12] for ethanol, the antifreeze properties of IPA lower the solidification temperature and increase the viscosity significantly, which slows the freezing front velocity.[29] Furthermore, water-IPA mixtures are believed to form clathrate hydrate structures,[29,30] in which the 'guest' IPA molecules are trapped by hydrogen bonding within an organized lattice of 'host' water molecules. **Figure 9** shows a phase diagram of the water-IPA system taken from Aladko et al.[29] As seen in the diagram, the concentrations of IPA used in this work (0–30 vol% or 0–37 wt%; red dots) all fall along the region corresponding to the clathrate structure: IPA-5H_2O. These clathrate hydrates, crystallized at temperatures below –50 °C, are composed of tetragonal unit cells (a = 0.640 nm, c = 1.116 nm).[29] The unit cells are folded into layers where the hydroxyl groups of the guest IPA molecules displace one of the water molecules in the lattice, leading to the elongated c-axis over that of the cubic clathrate.[29] Thus, the formation of these crystalline clathrate hydrates significantly increases the viscosity. The pore structures observed in Figure 7 must, therefore, be replicas of clathrate-like structures that form with the addition of IPA. Based on experimental results, an optimal

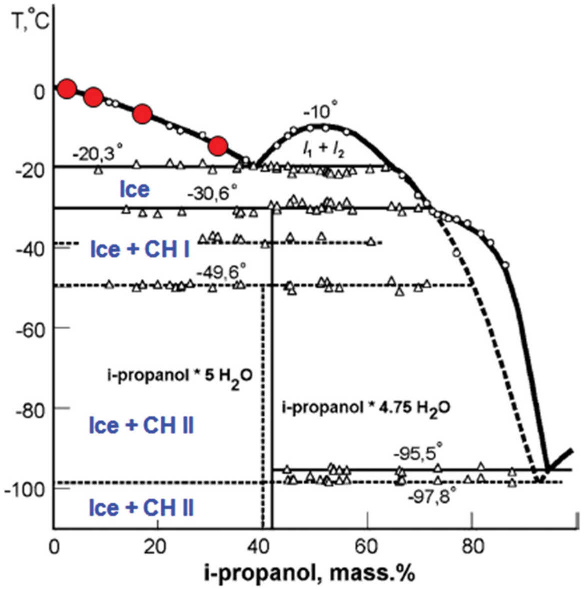

Figure 9. Phase diagram of the water-IPA system. The red dots represent the initial freezing points of the experiments carried out in this work for IPA concentrations of 0–30 vol% (corresponding to 0–37 wt% of the water-IPA solutions). The different mixtures of crystal structures existing in this system are shown in blue: ice, hexagonal ($a = 0.452$ nm, $c = 0.736$ nm); clathrate hydrate I (CH I), cubic (a = 1.256 nm); clathrate hydrate II (CH II), tetragonal ($a = 0.640$ nm, $c = 1.116$ nm). Adapted from Aladko et al.[29].

concentration of IPA is likely to exist around 5 vol%, where the formation of these layered or elongated hydrates seems most favorable.

The ranges of strength from 0.5–6.5 MPa and modulus from 100–800 MPa show that the dramatic increase in pore area and aspect ratio significantly reduces the compressive mechanical properties (see Figure 8). The changing pore morphologies resulting from changes in alcohol concentration reduce the mechanical performance of the scaffolds by a factor of ≈5; in contrast to the mechanical reduction by factors of ≈2 and ≈1.5 for the pH change and viscosity experiments, respectively. The decline in mechanical properties observed with the addition of alcohol (Figure 8b) may be due to the semi-uniform alignment and elongation of lamellar walls, which allow cracks to propagate through more easily as lamellae buckle under compression. Conversely, the smaller pore channels generated with no addition of alcohol (Figure 7a) distribute the load more evenly across the scaffold, putting less stress on each lamellae. Therefore, in agreement with Section 2.2, and as suggested by Hunger et al.,[9] smaller, low aspect ratio pores result in higher compressive properties by resisting the buckling of lamellar microstructures and subsequent crack propagation.

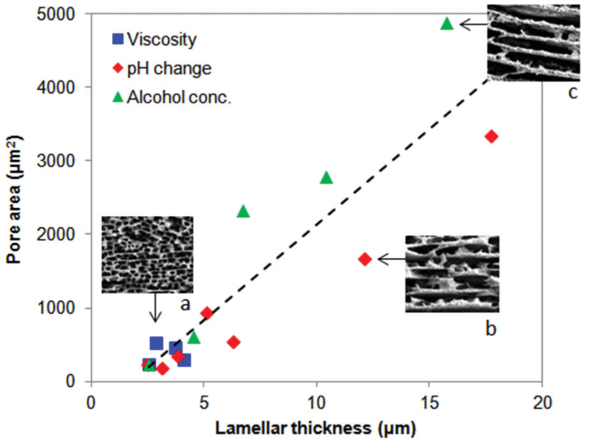

Figure 10. Comparison of TiO$_2$ scaffolds freeze cast with varying viscosity (blue, squares), pH change (red, diamonds), and alcohol concentration (green, triangles), illustrating an increasing trend for pore area versus lamellar thickness. Representative SEM images of TiO$_2$ scaffolds: a) 10 k PEG MW, pH 7, 0 vol% IPA; b) 10 k PEG MW, pH 4, 0 vol% IPA; c) 10 k PEG MW, pH 7, 5 vol% IPA. All SEM images shown are 250 µm wide.

2.5. Microstructure and mechanical properties

Figures 10,11 compare the lamellar thickness, pore area, aspect ratio, and compressive mechanical properties of all the scaffolds freeze cast with varying viscosity, pH, and alcohol concentration. As expected, a linear relationship between the pore area and lamellar thickness exists for all slurry conditions, despite the additive used (Figure 10). Obviously, at equal porosity, the pore area must increase as the lamellar thickness increases. The slight discrepancy between the pH change and alcohol concentration data, seen in Figure 10, is most likely due to the fact that water-IPA mixtures may form clathrate hydrate structures,[29,30] increasing the apparent pore sizes for respective lamellar thicknesses. Although the solidification time was not measured in this study, the lamellar thickness, and consequently the pore size, are expected to exhibit a similar direct correlation to the freezing front velocity as reported by Munch et al.[12] According to this work, the use of ethanol as an additive led to increased lamellar spacing, which is related to its relatively low solidification temperature, lengthening the phase to which the liquid and crystallized solid can coexist.[12] Our use of IPA as an additive provides evidence for this point, given that IPA-modified slurries resulted in larger pore areas and aspect ratios compared to scaffolds fabricated with varying viscosity or pH change. The low solidification temperature and the presence of intermolecular interactions (such as hydrogen bonding with IPA or increased local concentrations of additives due to the crystallization of water and clathrate hydrates) may affect the thermal properties of the newly-crystallized solid interface, as explained by Wegst et al.[18] Therefore, it is reasonable to assume that the different additives used to modify the rheological properties of the liquid slurries changed the temperature profile at which constitutional supercooling occurs, resulting in different freezing front velocities and consequent pore morphologies.

While no clear, comprehensive trend relating the lamellar thickness or pore area to the mechanical performance of the scaffolds was observed, a fairly strong empirical correlation between the pore aspect ratio and the compressive properties was found (see Figure 11). As seen in the plot (Figure 11a), both the strength and modulus show a rapid decay as the pore aspect ratio increases. As mentioned earlier, these results agree

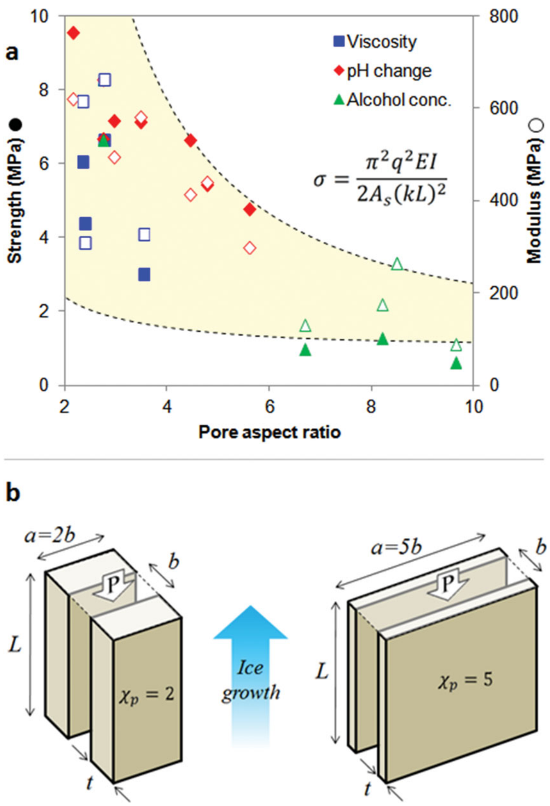

Figure 11. a) Comparison of the compressive mechanical properties versus pore aspect ratio of TiO_2 scaffolds freeze cast with varying viscosity (blue, squares), pH change (red, diamonds), and alcohol concentration (green, triangles). Solid markers correspond to compressive strength measurements, while hollow markers correspond to compressive modulus measurements. The decreasing quadratic trend shown in yellow is determined by the modified Euler buckling equation shown (σ), where the area moment of inertia (I) is a function of the pore aspect ratio (χ_p) (refer to Equations 8–12). b) Representative schematic drawings used to describe the simplified Euler buckling analysis (refer to Equations 8–12), where two lamellar walls of equal length (major axis) a, thickness t and height L, separated by a pore width (minor axis) b, are subjected to a compressive load P applied parallel to the wall height L. For the analysis, it is assumed that the representative specimens have constant lamellar wall heights ($L = 500$ µm), pore widths ($b = 15$ µm), and equal lamellar cross-sectional areas ($A_s = at$), but different pore aspect ratios (for example, left image: $\chi_p = 2$; right image: $\chi_p = 5$). For the range plotted above (yellow region in (a)), the lamellar wall cross-sectional area (A_s) was varied from 250 µm^2 to 1500 µm^2, which incorporates the majority of experimental measurements.

with Hunger et al.:[9] a decreased lamellar spacing (i.e., pore minor axis) and decreased pore aspect ratio lead to enhanced mechanical properties. This decreasing trend can be attributed to, not only the possibility for crack formation and growth due to local buckling of lamellar walls, but also the semi-uniform alignment of pore channels that distribute the load evenly across several lamellae. Moreover, an increased number of mineral bridges would decrease the apparent pore area and aspect ratio, yielding higher compressive mechanical properties. In response to compressive loading, mineral bridges prevent Euler buckling by hindering crack propagation through parallel lamellae.[12] Hence, the smaller and more uniform (i.e., low aspect ratio) the pores, the higher the mechanical properties—a function of the mechanisms that arrest local buckling of lamellae and subsequent crack propagation.

2.6. Euler Buckling Analysis

To further elucidate the effect of the aspect ratio on the local Euler buckling of the scaffolds, an analytical expression relating the compressive strength (σ) to the pore aspect ratio (χ_p) can be derived. Two idealized schematic representations are shown in Figure 11b to illustrate this phenomenon. This simplified model ignores the effect of mineral bridges and surface asperities. Keeping the total amount of material (i.e., lamellar wall cross-sectional area, $A_s = at$) and pore width (minor axis, b) constant, the pore aspect ratio can be increased by increasing the lamellar wall length (major axis, a) and correspondingly decreasing the lamellar wall thickness (t) (refer to Figure 11b). The Euler equation has the form[31]:

$$P = n^2 \frac{\pi^2 q^2 E I}{(kL)^2} \tag{8}$$

where P is the compressive load, n is the order of deflection (in our case, $n = 1$), E is the Young's modulus, I is the area moment of inertia, k is dependent on the geometry of the ends (in our case, $k = 0.5$ for fixed ends), and L is the lamellar wall height. In order to incorporate experimental unknowns, such as the internal wall porosity and surface roughness, an empirical factor q, dependent on the lamellar wall properties, was added into Equation 8. From the parallel axis theorem, the area moment of inertia is determined to be:

$$I = 2 \times \left(\frac{at^3}{12} + \frac{A_s}{4}(b+t)^2 \right) \tag{9}$$

By substituting $A_s = at$ and $\chi_p = a/b$ into Equation 9 and rearranging the variables, the area moment of inertia can be rewritten as a function of the pore aspect ratio (χ_p) in terms of the constants A_s and b:

$$I = \frac{2}{3}\frac{A_s^3}{b^2}\left(\frac{1}{\chi_p}\right)^2 + A_s^2\left(\frac{1}{\chi_p}\right) + \frac{A_s}{2}b^2 \tag{10}$$

The maximum compressive stress is $\sigma = P/2A_s$ and can be written as:

$$\sigma = \frac{\pi^2 q^2 E I}{2 A_s (kL)^2} \tag{11}$$

Finally, substituting in the area moment of inertia given by Equation 10 into the stress relation above, the maximum compressive stress is expressed as a function of the pore aspect ratio:

$$\sigma = \frac{\pi^2 q^2 E}{(kL)^2} \left(\frac{A_s^2}{3b^2}\left(\frac{1}{\chi_p}\right)^2 + \frac{A_s}{2}\left(\frac{1}{\chi_p}\right) + \frac{b^2}{4} \right) \tag{12}$$

To fit this modified Euler buckling equation (Equation 12 to the experimental data plotted in Figure 11a, several assumptions were made according to Figure 11b. First, the lamellar wall height and pore width (minor axis) were kept constant (equal to the averages of experimental measurements) at values of $L = 500$ μm and $b = 15$ μm, respectively. The Young's modulus of pure TiO_2, $E = 270$ GPa,[32] the geometric constant of $k = 0.5$, and the empirical correction factor of $q = 0.02$ were used to represent the stiffness and geometry of the lamellar walls. By setting the lamellar wall cross-sectional area equal to a range of $250\ \mu m^2 < A_s < 1500\ \mu m^2$, which incorporates the majority of experimental measurements, and plotting the stress (σ) as a function of the pore aspect ratio (χ_p), the quadratic trend shown in Figure 11a (yellow region) fits the experimental data quite well. Therefore, a simple modified Euler analysis incorporates the principal effects, suggesting that the primary failure mechanism in the TiO_2 scaffolds is local buckling followed by tensile cracking. The low value of q is an indication that the existing internal wall porosity and surface roughness introduce flaws that decrease the maximum stress considerably.

3. Conclusions

The effects of polyethylene glycol (PEG) viscosity, pH, and isopropanol alcohol (IPA) concentration on freeze cast TiO_2 scaffolds are compared. Porous ceramic scaffolds are achieved with varied properties such as pore size, coarse/fine surface features, alignment and spacing of lamellar walls, as well as bridging between pore channels. Relationships between porosity, lamellar thickness, pore morphology, compressive strength and modulus for each of these methods are reported. Altering the different slurry properties did not change the overall porosities of the scaffolds, but changed the pore morphologies significantly. In general, it is observed that smaller pore areas and aspect ratios provided increased strength and stiffness. A simplified analysis of Euler buckling predicts this trend in agreement with experimental results, where the strength of the scaffolds decreases as the aspect ratio of the pores increases, following a quadratic dependency.

The control of structure and mechanical properties achieved through the methods delineated above presents a bright potential for the creation of tailored scaffolds for bone replacement. The biocompatibility of TiO_2 is excellent and it is known to promote osteointegration. The control of pore size and aspect ratio is essential for cellular scaffolding and thus the methodology presented herein is eminently applicable for biomaterials. Applications needing a predefined porosity as well as requiring specified pore dimensions can be fulfilled by modifying the processing parameters of a freeze cast slurry. These parameters are readily available for control in the laboratory: its combination with TiO_2 may provide a base scaffolding compatible with biological materials and organisms.

4. Experimental Section

Sample Preparation: Aqueous slurries of 10 vol% TiO_2 (Sigma Aldrich, St. Louis, MO) powders (100–200 nm) were mixed with 1 wt% PVA (Alfa Aesar, Ward Hill, MA) and 1 wt% of an ammonium polymethacrylate anionic dispersant, Darvan 811 (R. T. Vanderbilt Company, Inc., Norwalk, CT). The three sets of aqueous slurries with different rheological properties were prepared by changing the following parameters: 1) viscosity: controlled by adding 1 wt% of PEG (Alfa Aesar, Ward Hill, MA) with varying molecular weights (0–20 000); 2) pH change: controlled by adding small amounts of 1 m HCl or NaOH (Fisher Scientific Inc., Waltham, MA) to respectively decrease or increase the slurry pH (2–12); 3) alcohol concentration: controlled by adding IPA (J.T. Baker, Center Valley, PA) of varying concentrations (0–30 vol%). The slurries with varying pH and alcohol concentration also contained 1 wt% PEG with a molecular weight of 10 000. All slurries were ball milled in an alumina grinding medium for 24 h, followed by degassing under low vacuum for 10–20 min. Approximately 10 mL of the degassed slurries were poured into a PVC mold and frozen at a constant rate of 10 °C min^{-1} using a custom built freeze casting device, as previously described.[25] After freezing, the samples were removed from the mold with a hydraulic press and lyophilized in a bench-top freeze dryer (Labconco, Kansas City, MO) at –50 °C and 350 Pa for 72 h. The porous green constructs were then sintered in an open air furnace for 3 h at 1000 °C with heating and cooling rates of 2 °C min^{-1}.

Slurry Properties: The pH of the aqueous slurries containing TiO_2 were measured with Alkacid pH test ribbons (Fisher Scientific Inc., Waltham, MA). The viscosity of the aqueous solutions were measured before adding the TiO_2 powders using a Gilmont falling ball viscometer (No. 2) with a glass ball (Thermo Fisher Scientific Inc., Waltham, MA). The viscosities (μ, mPa s) of the solutions were measured at 18 °C and calculated by: $\mu = K\ (\rho_b - \rho_l)\ t$, where $K = 3.3$ is the viscometer constant, $\rho_b = 2.53$ g mL^{-1} is the density of the glass ball, ρ_l is the measured density of the liquid, and t is the measured time of descent of the glass ball in min.

Material Characterization: X-ray diffraction (XRD) was performed on a Miniflex II XRD machine (Rigaku, Woodlands, TX). Scanning electron microscopy (SEM) images were taken at 15 kV on a Philips XL30 field emission environmental scanning electron microscope (FEI-XL30, FEI Company, Hillsboro, OR). For SEM preparation the samples were sputter-coated with iridium using an Emitech K575X sputter coater (Quorum Technologies Ltd., West Sussex, UK).

The average (± standard deviation) porosities of the scaffolds were calculated from eight samples each. The average pore size, geometry, lamellar thickness and interlamellar spacing of the scaffolds were measured from scanning electron micrographs using ImageJ software (National Institutes of Health, Bethesda, MD). To measure the pore size, the thresholds of the micrographs were adjusted equally such that the region of interest (i.e., pore area) could be selected and calculated from the major and minor axes of a fitted ellipse with an equivalent area and aspect ratio approximated by the software. The pore area (A_p) and pore aspect ratio (χ_p) reported here are the averages (± standard deviations) calculated from the elliptic major (a) and minor (b) axes from 40 selected pores each. The lamellar thickness (t) of the scaffold walls was averaged from 40 selected linear measurements each.

Mechanical Testing: Compression testing of the scaffolds was performed in an Instron materials testing machine (Instron 3342, Norwood, MA) with a 500 N load cell at a crosshead velocity of 0.005 mm s^{-1}. The scaffolds were cut into small samples of approximately 5 mm × 5 mm × 5 mm and compressed in the longitudinal, ice growth direction. To ensure testing of the homogeneous region and avoid the high-density regions of the scaffolds (i.e., the outer perimeter and the bottom 5 mm of the scaffold),[26] the samples were cut from the central core of the scaffolds (10 mm × 10 mm) between 5–30 mm from the bottom. The ultimate compressive strength and Young's modulus were determined from the maximum stress and the linear slope of the stress–strain curves, respectively. The average (± standard deviation) strength and modulus of the scaffolds were calculated from eight samples from each processing condition.

Acknowledgments

The authors would like to thank Dr. Antoni Tomsia at the Lawrence Berkeley National Laboratory for showing us his freeze casting setup.

This work is supported by the National Science Foundation, Division of Materials Research, Ceramics Program Grant, 1006931.

Received: August 23, 2013

---

[1] M. A. Meyers, J. McKittrick, P.-Y. Chen, *Science* **2013**, *339*, 6121.
[2] S. Deville, E. Saiz, R. K. Nalla, A. P. Tomsia, *Science* **2006**, *311*, 5760.
[3] E. Munch, M. E. Launey, D. H. Alsem, E. Saiz, A. P. Tomsia, R. O. Ritchie, *Science* **2008**, *322*, 5907.
[4] M. M. Porter, J. McKittrick, M. A. Meyers, *JOM* **2013**.
[5] S. Weiner, H. D. Wagner, *Annu. Rev. Mater. Sci.* **1998**, *28*.
[6] S. Lee, M. Porter, S. Wasko, G. Lau, P.-Y. Chen, E. E. Novitskaya, A. P. Tomsia, A. Almutairi, M. A. Meyers, J. McKittrick, in *MRS Online Proceedings Library* Vol. *1418*, Materials Research Society, Cambridge University Press, New York, NY, USA **2012**.
[7] S. Deville, *Adv. Eng. Mater.* **2008**, *10*, 3.
[8] W. L. Li, K. Lu, J. Y. Walz, *Int. Mater. Rev.* **2012**, *57*, 1.
[9] P. M. Hunger, A. E. Donius, U. G. K. Wegst, *Acta Biomater.* **2013**, *9*, 5.
[10] C. M. Pekor, P. Kisa, I. Nettleship, *J. Am. Ceram. Soc.* **2008**, *91*, 10.
[11] C. Pekor, B. Groth, I. Nettleship, *J. Am. Ceram. Soc.* **2010**, *93*, 1.
[12] E. Munch, E. Saiz, A. P. Tomsia, S. Deville, *J. Am. Ceram. Soc.* **2009**, *92*, 7.
[13] Q. Fu, M. N. Rahaman, F. Dogan, B. S. Bal, *Biomed. Mater.* **2008**, *3*, 2.
[14] S. Deville, C. Viazzi, C. Guizard, *Langmuir* **2012**, *28*, 42.
[15] Q. Fu, M. N. Rahaman, F. Dogan, B. S. Bal, *J. Biomed. Mater. Res. Part B* **2008**, *86B*, 1.
[16] Y. Zhang, K. Zhou, Y. Bao, D. Zhang, *Mater. Sci. Eng. C* **2013**, *33*, 1.
[17] J. L. Zou, Y. Zhang, R. X. Li, *Int. J. Appl. Ceram. Technol.* **2011**, *8*, 2.
[18] U. G. K. Wegst, M. Schecter, A. E. Donius, P. M. Hunger, *Philos. Trans. R. Soc. A* **2010**, *368*, 1917.
[19] S. Deville, E. Maire, G. Bernard-Granger, A. Lasalle, A. Bogner, C. Gauthier, J. Leloup, C. Guizard, *Nat. Mater.* **2009**, *8*, 12.
[20] S. Deville, E. Saiz, A. P. Tomsia, *Biomaterials* **2006**, *27*, 32.
[21] Q. Fu, M. N. Rahaman, F. Dogan, B. S. Bal, *J. Biomed. Mater. Res. Part B* **2008**, *86B*, 2.
[22] L. L. Ren, Y. P. Zeng, D. L. Jiang, *J. Am. Ceram. Soc.* **2007**, *90*, 9.
[23] L. Ren, Y.-P. Zeng, D. Jiang, *Ceram. Int.* **2009**, *35*, 3.
[24] L. Ren, Y.-P. Zeng, D. Jiang, *Solid State Sci.* **2010**, *12*, 1.
[25] M. M. Porter, M. Yeh, J. Strawson, T. Goehring, S. Lujan, P. Siripasopsotorn, M. A. Meyers, J. McKittrick, *Mater. Sci. Eng. A* **2012**, *556*.
[26] S. Deville, E. Saiz, A. P. Tomsia, *Acta. Mater.* **2007**, *55*, 6.
[27] K. A. Jackson, J. D. Hunt, *Transact. Metall. Soc. Aime* **1966**, *236*, 8.
[28] M. E. Glicksman, *Principles of Solidification*, Springer, New York, NY, USA **2011**.
[29] L. S. Aladko, A. Y. Manakov, A. G. Ogienko, A. I. Ancharov, *J. Incl. Phenom. Macrocycl. Chem.* **2009**, *63*, 1–2.
[30] S. S. N. Murthy, *J. Phys. Chem. A* **1999**, *103*, 40.
[31] F. P. Beer, J. E. Russell Johnston, J. T. DeWolf, *Mechanics of Materials*, McGraw-Hill, New York, NY, USA **2002**.
[32] J. Li, S. Forberg, L. Hermansson, *Biomaterials* **1991**, *12*, 4.